Design and modelling tools for DC HTS cables for the future railway network in France

Ghazi Hajiri, Kévin Berger, Rémi Dorget, Jean Lévêque, Hervé Caron

IOP Publishing Superconductor Science and Technology
Supercond. Sci. Technol. **35** (2022) 024003 (18pp) https://doi.org/10.1088/1361-6668/ac43c7

Design and Modelling tools for DC HTS cables for the future railway network in France

Ghazi Hajiri [1], Kévin Berger [1], Rémi Dorget [1,2], Jean Lévêque [1] and Hervé Caron [3]

[1] Université de Lorraine, GREEN, F-54000 Nancy, France
[2] Safran Tech, Electrical & Electronic Systems Research group, F-78114 Magny-Les-Hameaux, France
[3] SNCF Réseau, Directions Techniques Réseau, F-93418 La plaine Saint Denis, France

E-mail: ghazi.hajiri@univ-lorraine.fr

Received 31 August 2021, revised 3 December 2021
Accepted for publication 16 December 2021
Published 6 January 2022

Abstract

The use of High-Temperature Superconducting (HTS) cables in power systems increases transmission capacity whereas reducing the volume of the installation. In addition, in high current applications, HTS cables considerably reduce power losses, right-of-ways and total system mass. This paper presents different multi-physics studies to be performed to accuratly design the Direct Current (DC) HTS cables for the future railway network planned by the French company SNCF. The process used to design DC cables for high operating current (between 5 kA and 20 kA at 1750 V) made of commercial (RE)BaCuO tapes is presented. In this design process, the critical current density dependence $J_c(B, \theta, T)$ of the superconducting tapes, the thermal properties of the materials used as well as different cable cooling configurations are considered. Finally, we discuss the selection of the appropriate cooling configuration to ensure adequate cooling of the cable.

Keywords: superconducting cable, magnetic field, analytical calculation, direct current, cryogenics, thermal and hydraulic modelling

1. Introduction

The energy efficiency of the Rail Network (RN) is today a major issue, as it must respond to the reduction of CO_2 emissions following the new environmental reforms [1] and the increase in rail traffic. In addition, DC power systems are widely used in France and around the world [2–4]. On the other hand, it is becoming difficult to increase electrical power using conventional technologies in already densely urbanized areas. In fact, to avoid the problem of the voltage drop between substations [5], it requires the insertion of a transformer station near the most critical point of the line, which can impose constraints in densely populated areas.

To provide sufficient power to the operating network, it is necessary to transmit operating currents of up to 20 kA. For this purpose, the use of High-Temperature Superconducting (HTS) cables is particularly appropriate, since high powers can be transmitted without energy dissipation or voltage drop [6,7].In addition, this technology allows for cables with a much smaller cross-section than conventional resistive conductors, which considerably reduces constraints and costs [8], especially when it comes to design and civil engineering work on historic structures. The advantages of this technology do not end with the reinforcement of the RN, the superconducting cable also allows the relocation of substations outside urban areas [9]. Superconducting cables can be designed to protect the railway network in case of failure: e.g. short-circuit, overload [10].

In a previous study [11], an iterative procedure has been developed for the complete sizing of the DC superconducting cable for the RN. The sizing process and obtained results are based on the minimization of the total number of tapes with a 2D electromagnetic model. In such a case, where the determination of the twisting pitch of the tapes and the

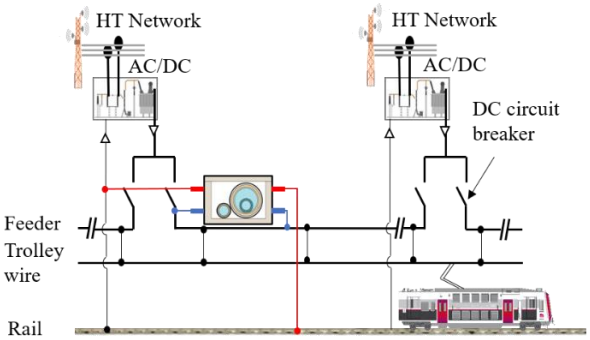

Figure 1. Typical diagram of the introduction of a bipolar DC superconducting cable in the railway network.

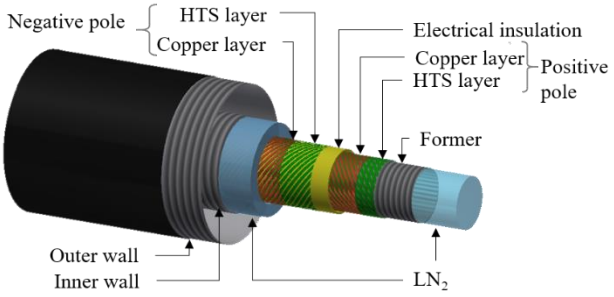

Figure 2. Complete view of a superconducting coaxial cable with its different layers.

calculation of the axial component of the magnetic field are not taken into account, the mass and total length of the tapes used in the cable may be underestimated. In addition, the steady state thermal model of the various cooling systems in [11] has not been fully covered. This is because the calculation of pipe heating as a function of length does not take into account the heat generated by the fluid flow in a pipe, as this assumption may not be appropriate for very long cables. In order to evaluate the force-free configuration in multilayer cables as a function of the longitudinal and transverse components of the magnetic field of each layer, other works [12] considers each layer of the superconducting cable as a closed cylinder, where the gap between the tapes of the same layer is not taken into account. Furthermore, 3D analytical models have been made to calculate the magnetic field created by an helical coil by neglecting the width and thickness of the tapes [13]. In addition, the Neumann formula has been used in [14–16] to develop analytical approximations of the self and mutual inductance of twisted tapes at a finite length.

This paper will focus on two main axes. The first part will present tools for multiphysics modelling in steady-state, including a 3D electromagnetic model to calculate the magnetic field, thermal and hydraulic models to study the performance of the cable. the second part will present a sizing and optimization method in which we try to minimize both the number of tapes per layer and per pole, as well as the hydraulic and cryostat losses. The algorithm also compares the different types of cooling. The different design steps are discussed, including the choice of the cryogenic line among which we find the following configurations: Separate Pipes (SP), Concentric Pipes (CP), Concentric Pipes with Separate Return (CPSR), and Concentric Pipes with Double Cooling Stations at Each End of the Cable (CPDS).

2. Modelling

2.1 HTS cable design

In DC rail applications, two superconducting cable topologies can be considered [17]. A superconducting cable with a positive pole is injected at one point of the line and the return current flows through the rail, or a superconducting cable with concentric positive and negative poles that supplies the forward and return current as shown in figure 1. A method for the design of DC superconducting cables is proposed below. The first part consists of identifying the critical current that must be higher than the transmission current by considering the different cable designs. For this, a 3D analytical model is proposed for the calculation of the magnetic field in the cable. The second part consists of a steady-state thermal and hydraulic study to keep the LN_2 temperature below 78 K with pressure above 3 bars [18]. All the parts mentioned above are coupled together in an iterative process to size the superconducting DC cable.

Depending on the topology of the cable, the DC HTS cable under consideration consists of one or two concentric poles. Each pole is composed of a certain number of layers. A layer indexed g consists of N_g tapes and the radius R_g of each layer is directly related to the number of tapes, the tape width d and the aperture between the tapes d_e. We want to calculate the magnetic field distribution produced by n rings of N_g tapes of each pole. Between the positive and negative pole, an electrical insulation layer is placed. Generally, kraft paper is used as a material because of its high dielectric strength of 50 kV/mm [19]. Finally, a cryostat wraps all these layers to maintain to keep the nitrogen in a liquid state. An example of the cable structure is shown in figure 2 for a bipolar topology with one layer per pole (n = 1).

2.2 Electromagnetic modelling

In this section, a 3D analytical model formulated in magnetic scalar potential using the variable separation method is presented. The model is flexible enough to perform two main tasks. The first one is to calculate the magnetic field in the cable to consider the dependence of the critical current on the magnetic field in the sizing process. The second task is to determine the self and mutual inductance of the tapes in order to evaluate the behavior in a dynamic regime. In this article, the calculation of the inductances will only be used to validate the model, as the proposed design process will not consider the transient regime.

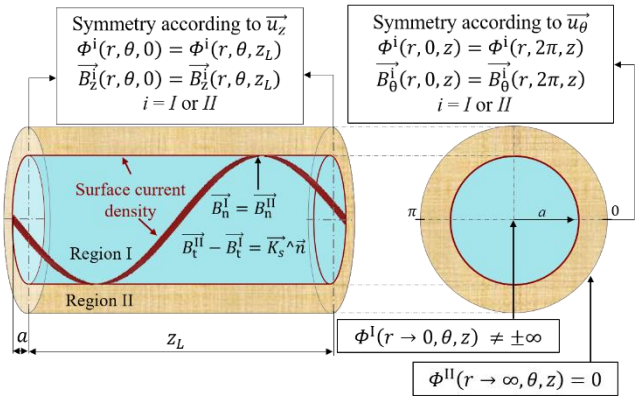

Figure 3. Section view of the problem with representations of the regions and boundary conditions. *t* and *n* represent the tangential and perpendicular component to the plane of the current sheet.

2.2.1 Assumptions and governing equations

The method used in this section allows the determination of the magnetic field created by a single layer of tapes. The determination of the total magnetic field generated by the cable is obtained by summing the contribution of each layer N_g. We assume the cable length to be infinite so we only need a single twist step to solve the electromagnetic problem. In order to simplify the electromagnetic problem, we assume that the total current is uniformly distributed between all the tapes of the cable. We also assume that the current density is uniformly distributed over a tape. Indeed, as was shown in [20], for an I/I_c ratio close to 1 the real current distribution is close to a uniform distribution. Since 2G HTS tapes have an important aspect ratio as the superconducting layer thickness is around 1 μm in thickness [21,22], the tapes are considered infinitely thin and the current density is therefore modeled as a surface current density [23]. Thus, the last assumption drastically simplifies the resolution as it is allowing us to solve the Maxwell's equations in scalar potential Φ instead of vector potential [24]. Additionally, there is one less volumetric region in which to calculate the magnetic field.

The determination of Φ is based on the solution of partial differential equations in cylindrical frame (r, θ, z). As shown in figure 3, the problem is divided into two regions, region ($i = I$) corresponds to ($r < a$) and region ($i = II$) corresponds to ($r > a$), with a is the radius of the current sheet, i is the index of each region and B is the magnetic induction. We formulate the Maxwell's equations in each region and solve:

$$\Delta\Phi^i = 0 \qquad (i = I \text{ or } II) \qquad (1)$$

$$\overrightarrow{B^i} = -\mu_0 \vec{\nabla}\Phi^i \qquad (i = I \text{ or } II) \qquad (2)$$

2.2.2 Boundary conditions

In this part, we define the boundary conditions required to solve the problem. In the radial direction, the Neumann conditions are used to avoid the divergence of the general solution at $(r \to 0)$ and $(r \to \infty)$ in the region I and II respectively. As shown in figure 3, due to the twisting effects of a 3D tape, the symmetry conditions are applied in the longitudinal $z \in [0, z_L]$ and azimuthal $\theta \in [0, 2\pi]$ direction.

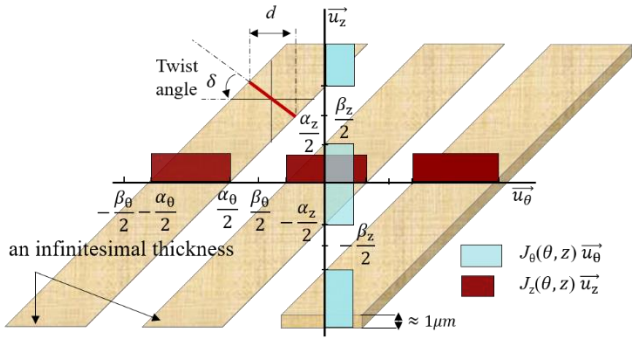

Figure 4. Representation of the two Fourier series decompositions of the helical current sheet.

$$\Phi^i(r \to 0,\theta,z) \neq \pm\infty \qquad (i = I) \qquad (3)$$

$$\Phi^i(r \to \infty,\theta,z) = 0 \qquad (i = I) \qquad (4)$$

$$\Phi^i(r,\theta,0) = \Phi^i(r,\theta,z_L) \qquad (i = I \text{ or } II) \qquad (5)$$

$$\Phi^i(r,0,z) = \Phi^i(r,2\pi,z) \qquad (i = I \text{ or } II) \qquad (6)$$

The process of solving expression 1 with the separation method and the general solution of Φ in each region is detailed in Appendix A. At the surface that separates the regions at $r = a$, we apply a surface current density $J_s(\theta,z)$ [A/m], as shown in figure 4, we define two spatial Fourier series decompositions to define the helical trajectory of the current sheet.

$$\overrightarrow{J_{s,r}}(\theta,z) = 0 \qquad (7)$$

$$\overrightarrow{J_{s,\theta}}(\theta,z) = \frac{J_{s,\theta Max}\,\alpha_z}{\beta_z} + \sum_{k=1}^{\infty} \frac{2J_{s,\theta Max}}{k\pi} \times \sin\left(\frac{\alpha_z}{\beta_z}\pi k\right) \cos\left(kN_g\left((\theta-\varphi_0) - \frac{2\pi}{z_L}z\right)\right) \qquad (8)$$

$$\overrightarrow{J_{s,z}}(\theta,z) = \frac{J_{s,zMax}\,\alpha_\theta}{\beta_\theta} + \sum_{k=1}^{\infty} \frac{2J_{s,zMax}}{k\pi} \times \sin\left(\frac{\alpha_\theta}{\beta_\theta}\pi k\right) \cos\left(kN_g\left((\theta-\varphi_0) - \frac{2\pi}{z_L}z\right)\right) \qquad (9)$$

where β_θ is the angular pitch and β_z is the axial pitch equal to $2\pi/N_g$ and z_L/N_g respectively, N_g is the number of tape of the layer g, α_z and α_θ are the apparent width and angle of the tape along the directions $\overrightarrow{u_z}$ and $\overrightarrow{u_\theta}$ and are equal to $d/\sin(\delta)$ and $d/(a\cos(\delta))$ respectively. a is the radius where the tapes are placed, d is the real width of the tape and δ is the twist angle.

The maximum values of each surface current density component $J_{s,\theta Max}$ and $J_{s,zMax}$ are equal to $I\sin(\delta)/d$ and $I\cos(\delta)/d$, where I is the total current flowing through the

Table 1. Analytical expression of the different components of the magnetic field in the two regions I and II. With $k' = k \times N_g$

	Region	Expression
B_r	I	$8\mu_0 N_g I \frac{a^2\pi}{d\, z_L{}^2} cos(\delta) \sum_{k=1}^{\infty} sin\left(\frac{\alpha_\theta}{\beta_\theta}\pi k\right) K'_{k'}(k'\, m\, a)\, I'_{k'}(k'\, m\, r)\, sin\left(k'\left((\theta-\varphi_0)-m\, z\right)\right)$
	II	$8\mu_0 N_g I \frac{a^2\pi}{d\, z_L{}^2} cos(\delta) \sum_{k=1}^{\infty} sin\left(\frac{\alpha_\theta}{\beta_\theta}\pi k\right) I'_{k'}(k'\, m\, a)\, K'_{k'}(k'\, m\, r)\, sin\left(k'\left((\theta-\varphi_0)-m\, z\right)\right)$
B_θ	I	$4\mu_0 N_g I \frac{a^2}{r\, d\, z_L} cos(\delta) \sum_{k=1}^{\infty} sin\left(\frac{\alpha_\theta}{\beta_\theta}\pi k\right) K'_{k'}(k'\, m\, a)\, I_{k'}(k'\, m\, r)\, cos\left(k'\left((\theta-\varphi_0)-m\, z\right)\right)$
	II	$\frac{\mu_0 N_g I}{2\pi r} + 4\mu_0 N_g I \frac{a^2}{r\, d\, z_L} cos(\delta) \sum_{k=1}^{\infty} sin\left(\frac{\alpha_\theta}{\beta_\theta}\pi k\right) I'_{k'}(k'\, m\, a)\, K_{k'}(k'\, m\, r)\, cos\left(k'\left((\theta-\varphi_0)-m\, z\right)\right)$
B_z	I	$\frac{\mu_0 N_g I}{z_L} - 8\mu_0 N_g I \frac{a^2\pi}{d\, z_L{}^2} cos(\delta) \sum_{k=1}^{\infty} sin\left(\frac{\alpha_\theta}{\beta_\theta}\pi k\right) K'_{k'}(k'\, m\, a)\, I_{k'}(k'\, m\, r)\, cos\left(k'\left((\theta-\varphi_0)-m\, z\right)\right)$
	II	$-8\mu_0 N_g I \frac{a^2\pi}{d\, z_L{}^2} cos(\delta) \sum_{k=1}^{\infty} sin\left(\frac{\alpha_\theta}{\beta_\theta}\pi k\right) I'_{k'}(k'\, m\, a)\, K_{k'}(k'\, m\, r)\, cos\left(k'\left((\theta-\varphi_0)-m\, z\right)\right)$

current sheet. The last required passage condition to solve the problem is at the boundary between the domains at $(r = a)$:

$$B_r{}^{II} = B_r{}^{I} \qquad (r = a) \qquad (10)$$

$$B_\theta{}^{II} - B_\theta{}^{I} = \mu_0 J_z \qquad (r = a) \qquad (11)$$

$$B_z{}^{II} - B_z{}^{I} = -\mu_0 J_\theta \qquad (r = a) \qquad (12)$$

Defining the surface current density as Fourier series allows to increase the flexibility of the model, as it is also possible to calculate the field created by a single tape. To do so, we can consider that only one tape is arranged on the layer *n*, in other words by imposing $N_g = 1$. By doing so, we can analyze the electromagnetic behavior of the cable more finely. An example for the tape inductance calculation will be given further in this article.

2.2.3 Magnetic field expression

In this section, we determine the expressions of the three components of the magnetic field. The solving procedure, the general solution and the identification of the parameters are detailed in appendix B. The contribution of the continuous current components $(J_{\theta Max}\, \alpha_z)/\beta_z\, \overrightarrow{u_\theta}$ and $(J_{zMax}\, \alpha_\theta)/\beta_\theta\, \overrightarrow{u_z}$ can be treated independently from the other components. Indeed, their contribution to the total magnetic field can be obtained by solving trivial magnetism problems. The component on θ corresponds to an infinite solenoid while the component on *z* corresponds to an infinite wire. Therefore, the calculation in the subdomains will only be used to compute the contribution of the surface current harmonics whereas the continuous components are calculated separately. Thus, in domains I and II the field created by the continuous components is directed along $\overrightarrow{u_\theta}$ and $\overrightarrow{u_z}$ respectively.

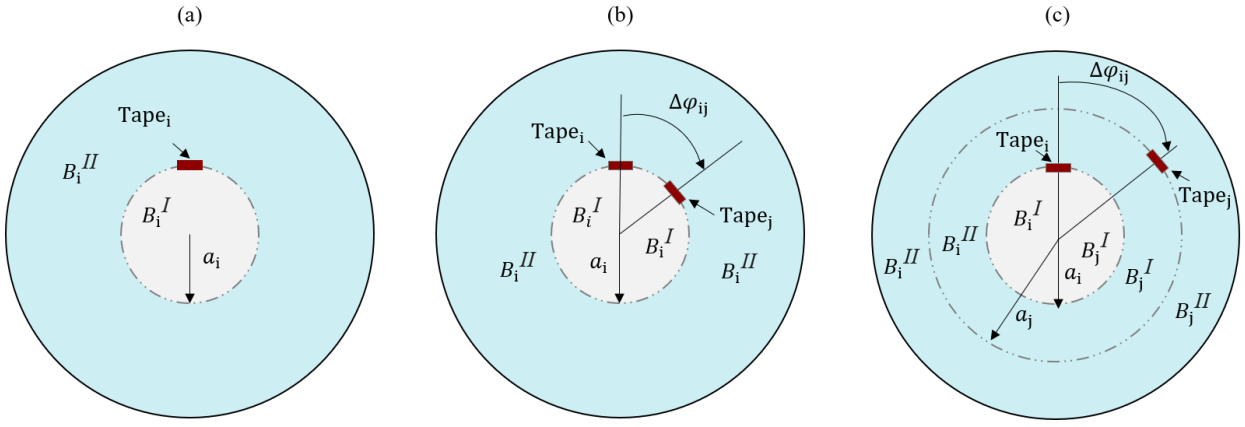

Figure 5. Representation of the magnetic field in each region, (a) calculation configuration of the self-inductance of a single tape, (b) calculation configurations of the mutual inductance between two tapes arranged on the same radius, (c) with different radii.

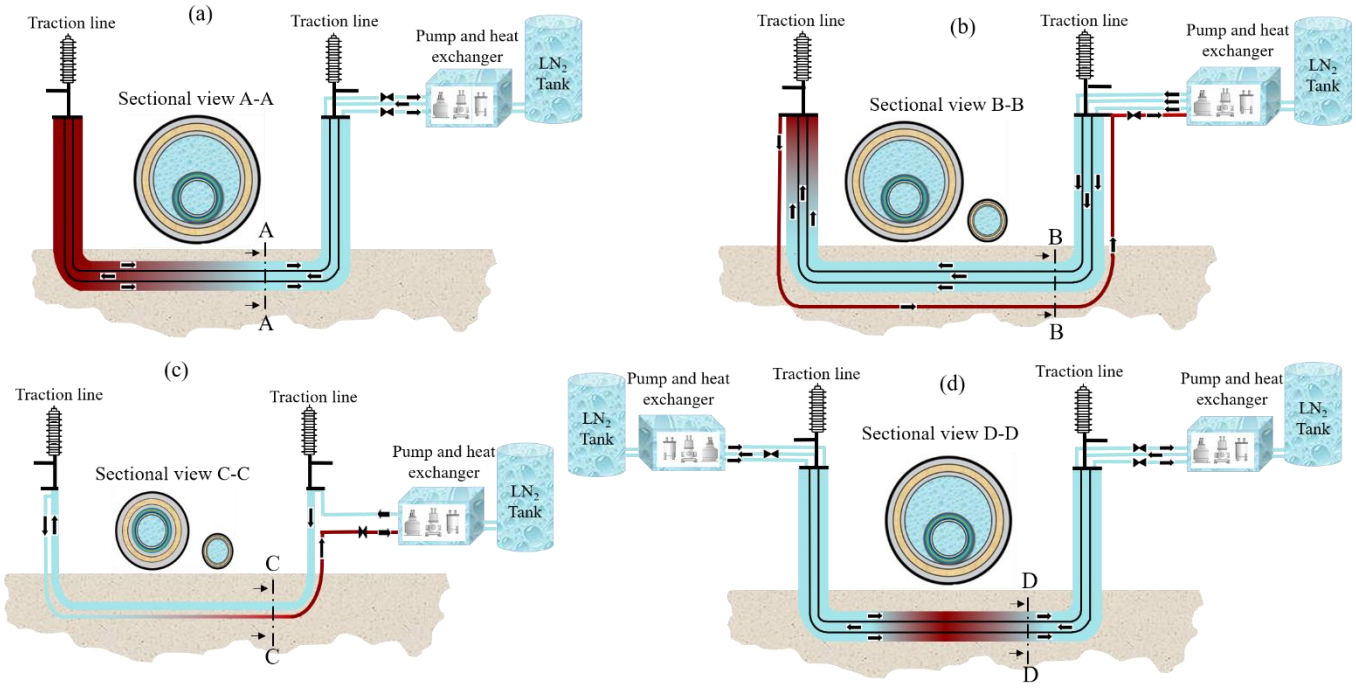

Figure 6. Typical schematic of superconducting cable introduction into the railroad system and Representation of cooling configurations: (a) Concentric pipes (CP), (b) Separate pipes (SP), (c) Concentric pipes with separate return (CPSR) and (d) Concentric pipes with two cooling systems at the ends of the cable.

The expressions of the magnetic field are shown in table 1, where $m=2\pi/z_L$ is the twist parameter, δ is the twist angle equal to atan$(a \times m)$. The initial position of tape is defined at ($r = a$, $\theta = \varphi_0$, $z = 0$). The solution of the problem in cylinders involves the modified Bessel functions of first kind I_k and second kind K_k. The function I'_k and K'_k represent the derivative of these functions respectively (see appendix B).

2.2.4 Self and mutual inductances

The values of the self and the mutual inductances are determined here by calculating the magnetic energy (W_m) obtained from a numerical integral over the whole volume ($\mathbb{R}^3$), where $dV = r\,dr\,d\theta\,dz$ with $r \in [0, R_{lim}]$, $\theta \in [0, 2\pi]$ and $z \in [0, z_L]$, with $R_{lim} \to +\infty$ (= 100 z_L) is the limit of the integral in the radial direction:

$$W_m = \frac{1}{2}\int_{\mathbb{R}^3} BH dV \tag{13}$$

where B and H are the magnetic flux density and the magnetic field. Due to the complexity of integrating the modified Bessel functions and in order to reduce the computational time, the previous expressions of the magnetic field can be integrated analytically along $\overrightarrow{u_\theta}$ and $\overrightarrow{u_z}$ and the integration along $\overrightarrow{u_r}$ can be solved numerically.

$$W_m = \frac{1}{2\mu_0}\left(\int_{\mathbb{R}^3} {B_i}^2 dV + \int_{\mathbb{R}^3} {B_j}^2\, dV + \int_{\mathbb{R}^3} 2B_iB_j\, dV\right) \tag{14}$$

$$W_m = \frac{1}{2}\left(L_iI_i + L_jI_j + 2L_{ij}I_iI_j\right) \tag{15}$$

As said above, the model can simulate a single twisted tape. Therefore, we can more finely analyze the inductance inside the cable. In particular, as shown in figure 5(a), by considering one layer with one tape ($N_g = 1$, $n = 1$), we can determine the self-inductance L_i of a single tape i using (14) in each region. The calculation of the mutual inductance L_{ij} of two tapes is obtained by integrating the scalar product of the magnetic field $B_i.B_j$ in each region. Two cases need to be distinguished. The first case where the two tapes are arranged on the same layer as shown in figure 5(b). In this case, the magnetic energy is the scalar product of the magnetic field created by the two tapes in the two regions, $\left(B_i^I \times B_j^I\right)$ at $(0 \le r \le a_i)$ and $\left(B_i^{II} \times B_j^{II}\right)$ at $(a_i \le r \le R_{lim})$. In the second case where the two tapes do not have the same radius, as shown in figure 5(c) the integral contains in three regions, $\left(B_i^I \times B_j^I\right)$ at $(0 \le r \le a_i)$, $\left(B_i^{II} \times B_j^I\right)$ at $(a_i \le r \le a_j)$ and $\left(B_i^{II} \times B_j^{II}\right)$ at $(a_j \le r \le R_{lim})$.

2.3 Hydraulic and thermal design (in normal operation)

Here, different configurations of superconducting cable cooling that can be employed are studied. Figure 6(a) shows the first configuration named concentric pipe (CP) consisting of two concentric liquid nitrogen pipes in a single cryostat and separated by superconducting tapes and an electrical insulator. The inner pipe leads the nitrogen from the station to the cable termination and the outer pipe brings the nitrogen back from

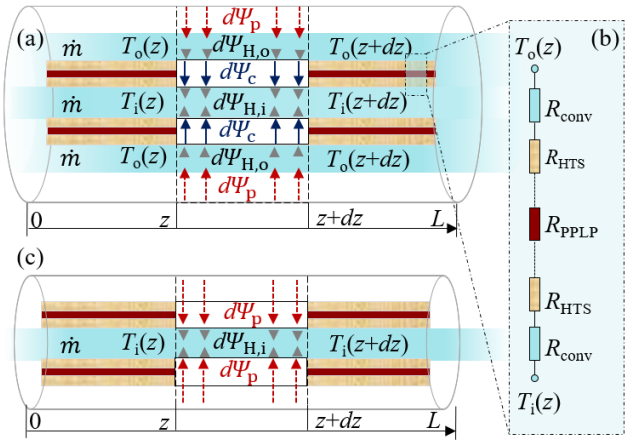

Figure 7. Simplified diagram of cooling type, (a) concentric configuration CP, (b) separate configuration SP,(c) A simple thermal conductance model to calculate the flux exchanged by convection and conduction between pipes through electrical insulation and tape layers. $T_o(z)$ is the temperature in the outer pipe and $T_i(z)$ is the temperature in the inner pipe. Ψ_p is the heat flux from the cryostat, Ψ_H is the heat flux related to hydraulic losses and Ψ_c is the heat flux transferred from the outlet pipe to the inlet pipe.

the termination to the cooling system. In figure 6(b), the second architecture Concentric Pipes with Separate Return (CPSR), it's composed of two concentric liquid nitrogen (LN_2) lines in a single cryostat as the CP configuration. The cable is thus located in these two pipes which transport the nitrogen from the station to the cable termination, while the nitrogen return pipe comprises no tapes. As shown in figure 6(c), the third architecture called Separated Pipes (SP) is composed of two separated lines, each with its own cryostat. The cable is placed in the pipe carrying the nitrogen from the station to the termination, while the pipe allowing the return of nitrogen does not carry any current. As shown in figure 6(d), the last architecture called Concentric Pipe with Double cooling Station at each end of the cable (CPDS), is composed of two concentric pipes in a single cryostat. The inner pipe conducts the liquid nitrogen (LN_2) from the first cooling system to the second and vice versa for the outer pipe.

2.3.1 Hydraulic study

The most important parameter affecting cable cooling is the LN_2 flow rate $\dot{m}$. However, it cannot be increased indefinitely, as it is not only restricted by the capacity of the system, but also by the pressure drops in the pipe Δp. In fact, the flow of a fluid in a longer pipe induces significant pressure drops that can cause nitrogen to leave its liquid state [25,26]. In order to manage these constraints, we will determine the pressure distribution in the pipes allowing for regular pressure drops. To perform this calculation, we use Bernoulli's theorem for each pipe [27]. We model the possible altitude variations by a function $H_a(z)$ which represents the altitude of each point of the cable. In addition, we model the pressure drops by the Darcy-Weisbach formula. The Darcy pressure drop coefficient will be determined by assuming that the pipe is smooth and using the Blasius correlation [28].

2.3.2 Thermal study

In this section, we determine the temperature of the pipes in steady-state along the length of the cable. For the thermal model of the DC HTS cable, only the hydraulic losses Ψ_H and the cryostat losses Ψ_p are considered. Hence, the loss flux of a cryostat wall Ψ_p is defined as:

$$d\Psi_P = 2\zeta_P dz \tag{16}$$

with $\zeta_p = \pi P_c R_c$, P_c is the surface loss in W/m^2 of the cryostat and R_c its outer radius. It is also assumed that the LN_2 temperature in a single pipe varies only along the length of the cable whereas the heat transfer between layers is only in the radial direction. For the hydraulic losses, the pressure drop caused by differences of altitude and the singular losses due to the turning points of the pipes are neglected [29]. Indeed, we are interested in calculating the regular losses generated by a straight cable at a finite length. this allows deducing that:

$$d\Psi_{H,s} = \dot{m}\, dp_{H,s} \tag{17}$$

$$dp_H = p_H(z+dz) - p_H(z)$$

where s is the index of the studied pipe, $\dot{m}$ is the mass flow rate in the z-direction in kg/s and dp is the regular pressure drop over an infinitesimal length dz. We therefore define:

$$dp_{H,s} = \frac{0.316\rho}{2R_F}\left(\frac{D_{H,s}}{\mu\pi {R_F}^2}\right)^{-0.25}\left(\frac{1}{\pi\rho {R_F}^2}\right)^2 m^{1.75}dz \tag{18}$$

with R_F is the normalized radius of the former, D_H is the hydraulic diameter of the pipe, ρ is the density and μ is the viscosity of the fluid. The expression of the hydraulic losses in W/m is the following:

$$d\Psi_{H,s} = \frac{0.316}{2\pi^2\rho^2 {R_F}^5}\left(\frac{D_{H,s}}{\mu\pi {R_F}^2}\right)^{-0.25} m^{2.75}dz \tag{19}$$

$$d\Phi_{H,s} = \chi_{H,s}\, m^{2.75}\, dz \tag{20}$$

For the rest of the paper, the CP, CPSR and CPDS configurations will be named CPxx for the sake of compacity. For CPxx configurations, as shown in figure 7(a), we note Ψ_p the heat flux transferred from the outlet pipe to the inlet pipe. The power absorbed by the liquid nitrogen in the outer pipe over an infinitesimal length dz is the difference between the power received from the cryostat losses $d\Psi_p$ plus the hydraulic losses $d\Psi_o$ and the flux transferred to the inner pipe $d\Psi_c$. Therefore, taking into account the flow direction of the nitrogen:

$$d\Psi_p + d\Psi_{H,o} - d\Psi_c = \mathrm{sgn}(\dot{m}_i\dot{m}_o)\dot{m}_o C_P dT_o$$
$$\mathrm{sgn}(\dot{m}_i\dot{m}_o) = 1 \quad \text{(for CPSR)}$$
$$\mathrm{sgn}(\dot{m}_i\dot{m}_o) = -1 \quad \text{(for CP, SP and CPDS)} \tag{21}$$

$$dT_o = T_o(z+dz) - T_o(z) \tag{22}$$

C_p is the heat capacity of LN_2. The subscripts i and o represent the inner and outer pipe respectively and T_o is the

outer pipe LN_2 temperature. The sign function $\mathrm{sgn}(\dot{m}_\mathrm{i}\dot{m}_\mathrm{o})$ is equal to +1 when inner and outer flow are in the same direction and to −1 for opposed flow directions. The energy conservation equation can also be written for the inner pipe LN_2 with T_i being the LN_2 temperature:

$$d\Psi_\mathrm{c} + d\Psi_\mathrm{H,i} = \dot{m}_\mathrm{i} C_\mathrm{P} dT_\mathrm{i} \tag{23}$$

$$dT_\mathrm{i} = T_\mathrm{i}(z + dz) - T_\mathrm{i}(z) \tag{24}$$

As shown in figure 7(b), a simple model is performed to calculate the flux exchanged by convection and conduction between the pipes through the electrical insulation and the layers of the tapes:

$$d\Psi_\mathrm{c} = G_0\big(T_\mathrm{o}(z) - T_\mathrm{i}(z)\big)\, dz \tag{25}$$

$$G_0 = \left(\begin{matrix} \dfrac{1}{h_\mathrm{i} 2\pi R_\mathrm{F,i}} \\ + \dfrac{1}{h_\mathrm{o} 2\pi R_\mathrm{F,o}} + \sum \dfrac{ln\left(\frac{R_q + th_q}{R_q}\right)}{2\pi K_q} \end{matrix} \right)^{-1} \tag{26}$$

G_0 is the equivalent thermal conductance per unit length, $R_\mathrm{F,i}$ and is the radius of the inner pipe, $R_\mathrm{F,o}$ is the radius of the outer pipe, k is the thermal conductivity of each layer, q is the index of each layer, h_i and h_o are the thermal convection coefficients of the inner and outer pipe respectively.

As shown in figure 7(c), the SP does not contain an external pipe, this case the losses from the cryostat are delivered directly to the internal pipe :

$$d\Psi_\mathrm{p,i} + d\Psi_\mathrm{H,i} = \dot{m} C_\mathrm{P} dT_\mathrm{i} \tag{27}$$

For the configurations comprising a return pipe (i.e. SP and CPSR), the temperature of the LN_2 return pipe is named T_r. The relation between the return pipre cryostat and T_r is identical to (26):

$$d\Psi_\mathrm{p,u} + d\Psi_\mathrm{H,u} = \dot{m} C_\mathrm{P} dT_\mathrm{u} \tag{28}$$

with index *r* represents the nitrogen return line which does not contain superconducting tapes. To solve these systems of equations, we apply the boundary conditions to each cooling configuration, here we assume that there is no loss at the cable termination. Indeed, at $z = L$, the temperatures of the inner and outer pipes of the CP configuration are equal. Since the CPDS configuration has two cooling systems at each end of the cable, the inner pipe temperature at ($z = 0$) and the outer pipe temperature at ($z = L$) are considered equal. For the CPSR configuration, the average value of the temperature of the two pipes is equal to the temperature of the liquid nitrogen return pipe at ($z = L$). Finally, for the SP configuration, the

Table 2. Expression of the polynomial coefficients of the different cooling configurations as a function of the geometric parameters and the thermal properties of the materials, with $T_\mathrm{i}(0)$ represents the inlet temperature of LN_2, $T_\mathrm{i}(0) = 68$ K.

Cooling configuration	Pipe	Expression
CP	$T_\mathrm{i}(z)$	$-\dfrac{G_0(\zeta_\mathrm{P} + \chi_\mathrm{i} + \chi_\mathrm{o})}{(\dot{m}C_\mathrm{p})^2} z^2 + \left(\dfrac{LG_0(2\zeta_\mathrm{P} + \chi_\mathrm{i} + \chi_\mathrm{o})}{(\dot{m}C_\mathrm{p})^2} + \dfrac{\chi_\mathrm{i}}{\dot{m}C_\mathrm{p}}\right) z + T_\mathrm{i}(0)$
	$T_\mathrm{o}(z)$	$-\dfrac{G_0(\zeta_\mathrm{P} + \chi_\mathrm{i} + \chi_\mathrm{o})}{(\dot{m}C_\mathrm{p})^2} z^2 + \left(\dfrac{LG_0(2\zeta_\mathrm{P} + \chi_\mathrm{i} + \chi_\mathrm{o})}{(\dot{m}C_\mathrm{p})^2} - \dfrac{2\zeta_\mathrm{P} + \chi_e}{\dot{m}C_\mathrm{p}}\right) z + \dfrac{L(2\zeta_\mathrm{P} + \chi_\mathrm{i} + \chi_\mathrm{o})}{\dot{m}C_\mathrm{p}} + T_\mathrm{i}(0)$
CPSR	$T_\mathrm{i}(z)$	$\dfrac{(2\zeta_\mathrm{P} + \chi_\mathrm{i} + \chi_\mathrm{o})}{2\dot{m}C_\mathrm{p}} z + \dfrac{4G_0T_\mathrm{i}(0) - 2\zeta_\mathrm{P} + \chi_\mathrm{i} - \chi_\mathrm{o}}{4G_0}\left(1 - e^{-\frac{2G_0}{\dot{m}C_\mathrm{p}}z}\right) + T_\mathrm{i}(0) e^{-\frac{2G_0}{\dot{m}C_\mathrm{p}}z}$
	$T_\mathrm{o}(z)$	$\dfrac{(2\zeta_\mathrm{P} + \chi_\mathrm{i} + \chi_\mathrm{o})}{2\dot{m}C_\mathrm{p}} z + \dfrac{4G_0T_\mathrm{i}(0) - 2\zeta_\mathrm{P} + \chi_\mathrm{i} - \chi_\mathrm{o}}{4G_0}\left(e^{-\frac{2G_0}{\dot{m}C_\mathrm{p}}z} - 1\right) + T_\mathrm{i}(0)\left(2 - e^{-\frac{2G_0}{\dot{m}C_\mathrm{p}}z}\right)$
	$T_\mathrm{u}(z)$	$-\dfrac{2\zeta_\mathrm{u} + \chi_\mathrm{u}}{\dot{m}C_\mathrm{p}} z + \dfrac{L(2\zeta_P + 4\zeta_\mathrm{u} + \chi_\mathrm{i} + \chi_\mathrm{o} + 2\chi_\mathrm{u})}{2\dot{m}C_\mathrm{p}} + T_i(0)$
SP	$T_\mathrm{i}(z)$	$\dfrac{2\zeta_\mathrm{P} + \chi_\mathrm{i}}{\dot{m}C_\mathrm{p}} z + T_\mathrm{i}(0)$
	$T_\mathrm{u}(z)$	$-\dfrac{2\zeta_\mathrm{u} + \chi_\mathrm{u}}{\dot{m}C_\mathrm{p}} z + \dfrac{L(2\zeta_\mathrm{P} + 2\zeta_\mathrm{Pr} + \chi_\mathrm{i} + \chi_\mathrm{u})}{\dot{m}C_\mathrm{p}} + T_\mathrm{i}(0)$
CPDS	$T_\mathrm{i}(z)$	$-\dfrac{G_0(\zeta_\mathrm{P} + \chi_\mathrm{i} + \chi_\mathrm{o})}{(\dot{m}C_\mathrm{p})^2} z^2 + \left(\dfrac{{G_0}^2L^2((\zeta_\mathrm{P} + \chi_\mathrm{i} + \chi_\mathrm{o}))}{(\dot{m}C_\mathrm{p})^2(\dot{m}C_\mathrm{p} + G_0L)} + \dfrac{LG_0((2\zeta_\mathrm{P} + \chi_\mathrm{o}))}{\dot{m}C_\mathrm{p}(\dot{m}C_\mathrm{p} + G_0L)} + \dfrac{\chi_\mathrm{i}}{\dot{m}C_\mathrm{p}}\right) z + T_\mathrm{i}(0)$
	$T_\mathrm{o}(z)$	$-\dfrac{G_0(\zeta_\mathrm{P} + \chi_\mathrm{i} + \chi_\mathrm{o})}{(\dot{m}C_\mathrm{p})^2} z^2 + \left(\dfrac{{G_0}^2L^2(\zeta_\mathrm{P} + \chi_\mathrm{i} + \chi_\mathrm{o})}{(\dot{m}C_\mathrm{p})^2(\dot{m}C_\mathrm{p} + G_0L)} + \dfrac{G_0L(2\zeta_\mathrm{P} + \chi_\mathrm{o})}{\dot{m}C_\mathrm{p}(\dot{m}C_\mathrm{p} + G_0L)} - \dfrac{(2\zeta_\mathrm{P} + \chi_\mathrm{o})}{\dot{m}C_\mathrm{p}}\right) z + \dfrac{G_0L^2(\zeta_\mathrm{P} + \chi_\mathrm{i} + \chi_\mathrm{o})}{\dot{m}C_\mathrm{p}(\dot{m}C_\mathrm{p} + G_0L)} + \dfrac{L(2\zeta_\mathrm{P} + \chi_\mathrm{o})}{(\dot{m}C_\mathrm{p} + G_0L)} + T_\mathrm{i}(0)$

temperature of the onward pipe is equal to the temperature of the return pipe at ($z = L$).

$$T_o(L) = T_i(L) \quad \text{(for CP)} \quad (29)$$

$$T_o(L) = T_i(0) \quad \text{(for CPDS)} \quad (30)$$

$$T_u(L) = \langle T_i(L) + T_o(L) \rangle \quad \text{(for CPSR)} \quad (31)$$

$$T_u(L) = T_i(L) \quad \text{(for SP)} \quad (32)$$

From these boundary conditions, we deduce the LN_2 temperature along each pipe by integration of (21), (23), (27) and (28). The temperature expressions for each case are expressed in table 2.

In the model presented above, the joule losses related to the *di/dt* variation of the current are neglected. Indeed, in a DC HTS cable dedicated to railway applications, they represent a few tens of mW/m, i.e. at most about 1% of the cryostat losses. (not reported here). Moreover, it would possible to adapt the thermal model for the study of AC cables by inclunding the AC losses in equations (21) (23) and (27).

3. Sizing process

This section describes the sizing and optimization process of superconducting DC cables. Based on the electrical parameters of the French railway network, a nominal voltage of 1500 V, a carrying current between 5 kA and 20 kA and the length of the cable, the algorithm tries to determine the best cable topology whereas minimizing the total length of tape used and the hydraulic and cryostat losses. Second-generation (2G) superconducting tapes are used here [30], their width is 4 mm and their thickness is about 200 µm, the thickness of the substrate and the copper layer is equal to 100 µm and 75 µm respectively. The international standard DIN EN10380, which specifies the minimum requirements for the manufacture of corrugated and flexible metal tubes, has been considered. The first step of the algorithm is to build the cable geometry based on the normalized radius of the former R_F ($g = 0$) and the number of layers per pole n. As shown in figure 8, the radius of each layer per phase is defined as follows:

$$R_{g+1} = R_F + th_p + g.th_{Tape} + \vartheta.th_{PPLP} \quad \begin{pmatrix} \vartheta = 0 \text{ for } g \le n \\ \vartheta = 1 \text{ for } g > n \end{pmatrix} \quad (33)$$

when $g = 1$ the radius of the first layer of the cable is equal to the normalized radius plus its wall thickness th_p, th_{Tape} is the thickness of the superconducting tape, th_{PPLP} is the thickness of the electrical insulator between the positive and negative poles, ϑ is coefficient is equal to 0 or 1 to consider the thickness of the electrical insulator for the calculation of the negative pole radius.

For CPxx configurations, we try to keep the nitrogen velocity constant between the two pipes. In other words, the cross-sectional areas of the two pipes through which the fluid passes are equal, which leads us to express the radius R_e ($g = 2n+1$) as a function of R_F:

$$R_e = \sqrt{2R_F{}^2 + 2e_i R_F + e_i{}^2} \quad (34)$$

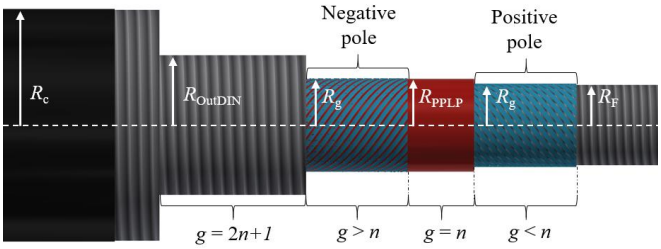

Figure 8. Representation of the different radii of a bipolar DC superconducting cable.

e_i representing the sum of the thickness of all the layers with the electrical insulation. In order to determine the normalized radius of the external pipe R_{OutDIN}, we choose the value slightly superior or equal to R_e. The second step is to determine the maximum number of tapes for each layer per pole N_i. This depends mainly on the maximum distance between tapes of the same layer d_e, the twist angle δ and the radius where the tape is located using the following formula:

$$N_i = \frac{2\pi R_g}{\frac{d}{\cos(\delta_g)} + d_e} \quad (35)$$

To determine the critical current, we use the Kim-Anderson model [31] which provides a relationship between the critical current of a tape and the norm B and angle $\theta = \arctan(B_{//}/B_{\perp})$ of the applied magnetic field for a given temperature T:

$$I_c(B_{//}, B_{\perp}, T) = \frac{I_{c0}(T)}{\left(1 + \frac{\sqrt{k_a{}^2 B_{//}{}^2 + B_{\perp}{}^2}}{B_0}\right)^{\sigma}} \quad (36)$$

with $I_{c0}(T)$ the critical current under zero field for a given temperature, k_a is the anisotropy factor determined using the angular dependence of the tape considered, B_0 and σ are the constants that characterize the variation of I_c according to the applied magnetic field. The values of these parameters are obtained from fitting experimental data provided in [32,33].

Two important points are to be noted here. First, the equation (36) uses the value of the parallel and perpendicular components of the flux density whereas the data are provided as function of the flux density norm and angle. However, it is easy to link these parameters to each other by $B_{//} = B\sin(\theta)$ and $B_{\perp} = B\cos(\theta)$ with $\theta = 0$ corresponds to the field perpendicular to the tape surface. Second, one should remember that the experimental data provide the value of the critical current of a tape as a function of a magnetic field applied by an additional source of magnetic field, which means that the self-magnetic field of a tape being studied should not be accounted while determining its critical current. Thus, in the cable, to determine the critical current of a tape, it is necessary to compute the magnetic field generated by all the tapes of the cable except the studied tape.

In order to include T_{LTmax}, the temperature dependence of the current density has been considered using a linear relation [31]:

$$I_{\mathrm{c0}}(T_{\mathrm{LTmax}}) = I_{\mathrm{c0,68\ K}}\left(\frac{T_{\mathrm{c}} - T_{\mathrm{LTmax}}}{T_{\mathrm{c}} - 68\ \mathrm{K}}\right) \qquad (37)$$

T_{c} is the critical temperature of the superconducting material and $I_{\mathrm{c0,68\ K}}$ is the critical current density at 68 K for zero applied field on the tape.

Here the total critical current I_{c} value is fixed and equal to 1.2 I_{n} with I_{n} being the transport current, here a sizing margin of 20% has been chosen to take into account the inhomogeneity of the critical current density according to the cable length [34]. If the T_{LTmax} value is lower than the liquid nitrogen inlet temperature 68 K, the studied cable configuration cannot be a solution, i.e. the cable must be cooled more to ensure a total critical current higher than the transport current. If T_{LTmax} is higher than 68 K, we use the parameters shown in table 2 to check that the cooling system can ensure the cooling T_{LTmax} while maintaining the liquid nitrogen in our operating area, 68 K $\leq T_{\mathrm{LN2}} \leq$ 78 K and 3 bar $\leq p \leq$ 15 bar.

It should be noted that this method represents a single study of a single cable. At the end of the analysis, the algorithm calculates multiple iterations for each normalized radius and the different number of layers per pole to determine the best cable configuration. In addition, this sizing method was applied to the four cooling systems shown in figure 6. Furthermore, the algorithm seeks to determine the best cable topology whereas minimizing the total length of the tapes and as well as the hydraulic and cryostat losses.

4. Results

4.1 Validation of the analytical model

In this section, a validation and an evaluation of the performance of the previously presented model is made through a comparison between the following two methods:

- An analytical magnetic scalar potential model (Φ- Model) where the magnetic fields are obtained from the expressions of table 1 where the calculation of the self and mutual inductance is obtained by numerical integration on the Matlab software.
- A model using the COMSOL-Multiphysics software (COMSOL) using an A-formulation where the calculation of the self and mutual inductance is obtained by the integral over the tape surface of the scalar product of the vector potential and the surface current density.

As shown in figure 9, the tape mesh is free-triangle with a maximum element size of 0.1 mm. The air around the tape has been meshed in free tetrahedral with a normal size. The tape used has a width d = 12 mm and an infinitesimal thickness, the winding radius a = 30 mm and a twist pitch z_{L} = 300 mm. As shown in figure 9, the ring carries five tapes displaced by an angle of 32.14°. A current of 100 A flows through each tape. An early comparison of the two models is made along the L_1 cut line.

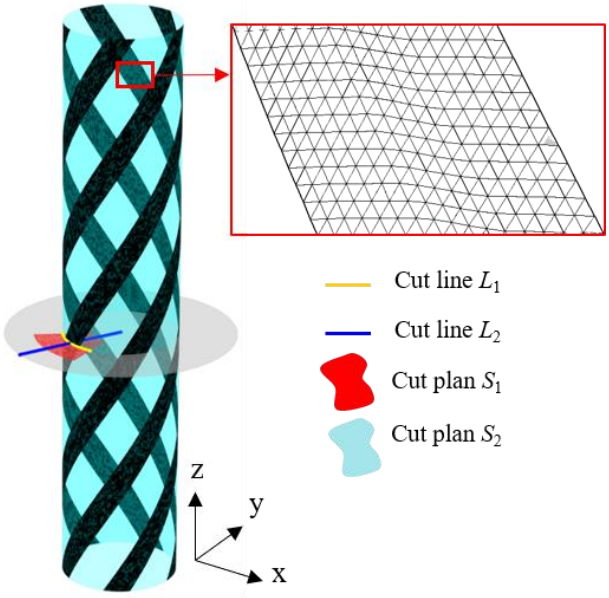

Figure 9. Schematic view of five coaxial helical conductor tapes with thin arc-shaped cross section and 300 mm twist pitch, the mesh of the tapes and the representation of the different surfaces and the model comparison cut line at ($r = a$, θ, $z_{\mathrm{L}}/2$).

According to the parameters in Table 3, the components of the magnetic field B_{r}, B_{θ} and B_{z} as well as the norm of B for different harmonic numbers N_{b} are presented in figure 10. First, we find the usual forms of the three components of the magnetic field. It appears that the number of harmonics has a great impact on the model accuracy. Moreover, the critical current calculation depends on the maximum value of the field applied on tape. This requires the use of a large number of harmonics in the sizing process to be precise enough on the radial component of the magnetic field. For this reason, to reduce the computational time and to avoid the numerical problems associated with modified high-order Bessel functions, we use the expressions of table 1 for the calculation of the field of a single tape (N = 1). The magnetic field created by a complete ring is obtained by rotating the tapes with respect

Table 3. Parameters used for the comparison between models.

Parameter	Value	Unit
d	12	mm
z_{L}	300	mm
a	30	mm
δ	32.14	°
n	1	---
N	1	---
R_{lim}	10z_{L}	mm

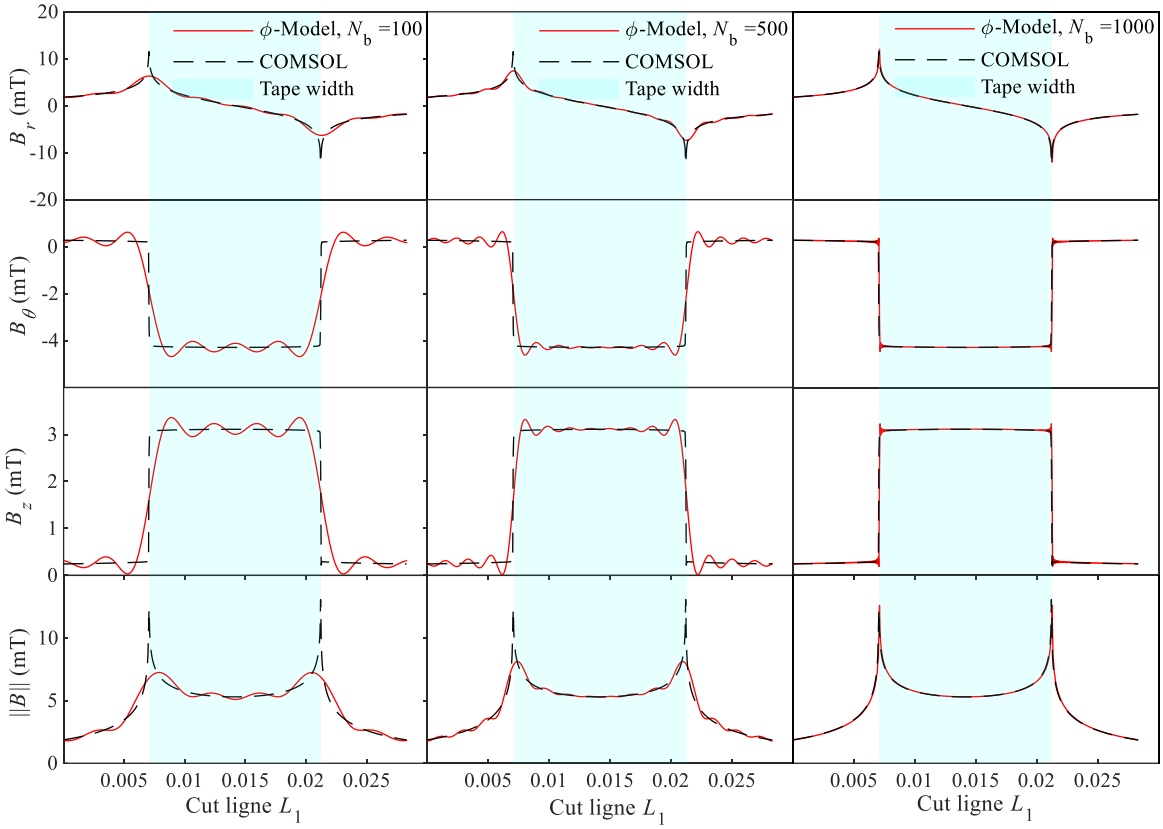

Figure 10. Comparison of B_r, B_θ, B_z and Norm$B$ between Φ-Model and A-Formulation (COMSOL) for different harmonic numbers N_b along the L_1 cut line, for $N = 1$.

to the center of the cable, with a rotation angle equal to $2\pi/N_t$, where N_t is the total number of tapes in the ring. Thus, the calculation of the total field requires as many iterations as there are tapes in the cable, but the reduced number of harmonics still allows this process to be faster.

In order to validate the behavior of the model in the two regions, figure 11 illustrates the two tangential components B_θ and B_z along the cut line L_2 respectively. We note that the correspondence between the two models is present at N_b equal to 50. Moreover, in figure 11 and at the boundary between the two regions (a = 30 mm), we find the discontinuity of the two tangential components due to the surface current density.

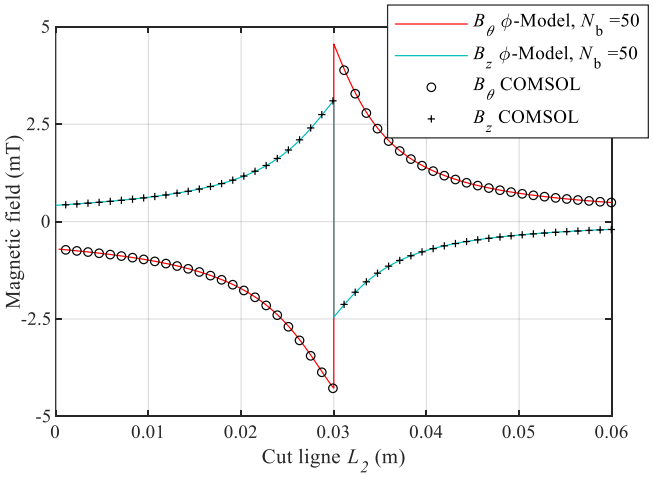

Figure 11. The two tangential components of the magnetic field B_θ and B_z along the cut line L_2, for $N = 1$.

From these results, we conclude that a very high harmonic number is required for the determination of the local magnetic field in the tape region whereas the distribution in the space around requires much fewer harmonics. In spite of these constraints on the harmonic number, the Φ-Model remains much faster than the A-Formulation (COMSOL), in fact, the Φ-Model gives the solution in about 0.2 ms and 10 ms respectively for a N_b of 100 and 1000 respectively while the A-Formulation (COMSOL) requires about 15 minutes for a single tape whereas modelling the complete cable in 3D on FEM is extremely costly in terms of computation time.

4.2 Self and mutual inductances

Here, we are interested in studying the variation of the inductance of a superconducting tape with the tape twist angle. Figure 12 shows the variation of self-inductance of a superconducting tape as a function of the torsion angle. Note that the tape is 4 mm wide, the harmonic number N_b = 50, the winding radius is fixed a = 30 mm. It can be seen from figure 12 that we have a good correspondence between the two models. Moreover, the value of the inductance becomes

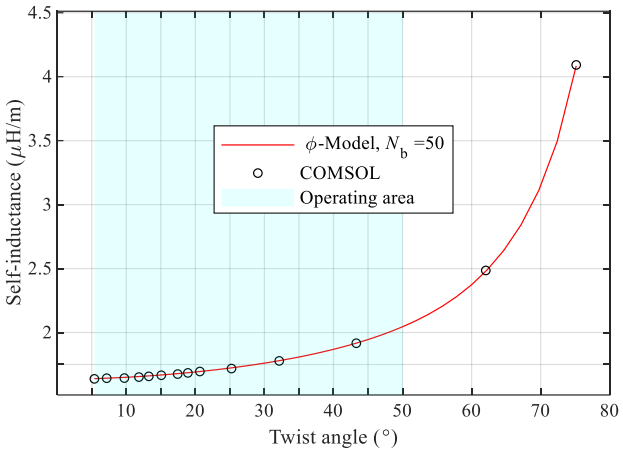

Figure 12. Self-inductance as a function of the twist angle, radius a = 30 mm.

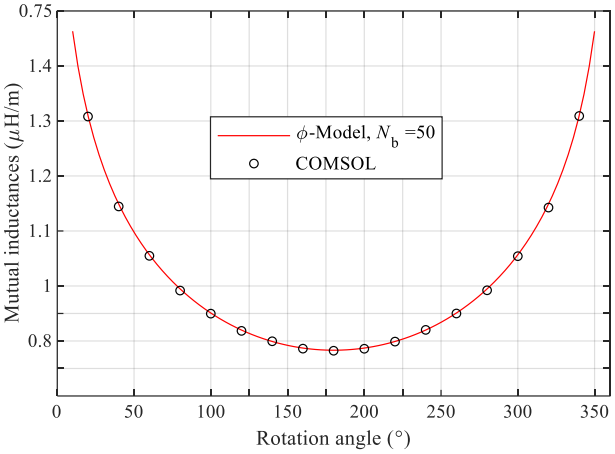

Figure 13. Mutual inductance between two tapes on the same layer as a function of the rotation angle $\Delta\varphi_{ij}$ with twist angle δ = 32.14 °.

significant from a torsion angle of 50° degrees, i.e. where we approach the case of a coil. On the other hand, when the torsion angle is between 5° and 50° degrees, the inductance does not undergo a significant variation, in the case of the simulation, a difference of about 0.4 µH/m between 5° and 50° (green area) and a difference of 2.2 µH/m between 50° and 78°.

Figure 13 shows the variation of the mutual inductance between two tapes of the same layer as a function of the phase shift angle $\Delta\varphi_{ij}$. The first tape is fixed and is located at ($r = a$, $\theta = 0$, $z = 0$) and the second tape is mobile and located at (r = a, $\theta = \Delta\varphi_{ij} \in [0, 2\pi]$, $z = 0$), in this study we have kept the same radius as in the self-inductance case, the pitch of the twist is z_L = 100 mm, and a twist angle is 32.14°. We notice symmetry of the results at $\Delta\varphi_{ij}$ = 180°, this point represents the maximum distance between the two tapes or L_{12} = 0.78 µH/m.

Figure 14 shows the variation of the total inductance of a layer of a superconducting cable as a function of the number of tapes for different winding diameters Normalized DIN10380, here the twist pitch is 250 mm and the pipe diameters are 25 mm, 32 mm and 40 mm, i.e. a twist angle equal to 17.44°,

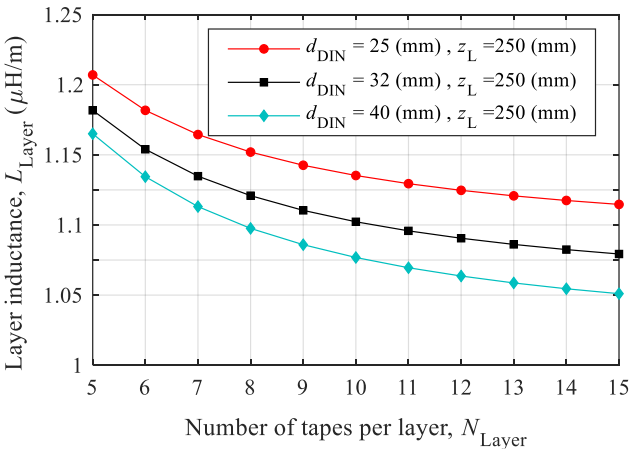

Figure 14. The influence of the number of tapes N_{Layer} on the total inductance of the layer L_{Layer}.

21.90° and 26.68° respectively. We observe that the self-inductance of the layer L_{Layer} is lower when increasing the radius, as an example, for a layer of 10 tapes, we have L_{Layer} = 1.13, 1.10 and 1.07 µH/m for the standardized diameter of 25, 32 and 40 mm respectively, Moreover, the total inductance of a layer decreases with the number of tapes, in fact for the normalized diameter d_{DIN} = 40 mm the inductance of the layer is equal to 1.16 µH/m for N_{Layer} = 5 and equal to 1.05 µH/m for N_{Layer} = 15.

In a DC superconducting cable for railway applications, a layer contains a few dozen superconducting tapes per layer [4]. From these results, we can deduce that the number of tapes does not have a significant influence on the total inductance of the cable. Moreover, twisting the tapes in a DC superconducting cable has two main interests. The first one is purely mechanical, in order to respect the limits of the tape-twisting machine and to ensure good flexibility of the cable. The second one is to obtain a homogeneous distribution of the current in the dynamic regime between the layers of the cable [35,36]. This requires an adaptation of the twisting pitch of each layer according to its radius in order to obtain an almost identical mutual inductance between the layers. Finally, the twisting pitch has a significant influence on the total length of the tape to be used, and therefore on the cost of the cable. In a superconducting cable, the twist angle generally varies between about 5 and 50 degrees [37,38].

4.3 Thermal and hydraulic study

Following the expressions in table 2, figure 15 shows the steady-state temperature profile of the pipes for different superconducting cable cooling topologies. The geometrical parameters of the superconducting cable are given in table 4, the values of the physical properties are shown in table 5, the mass flow rate $\dot{m}$ is 0.6 kg/s and the cryostat losses per unit of surface P_c is equal to 3 W/m^2.

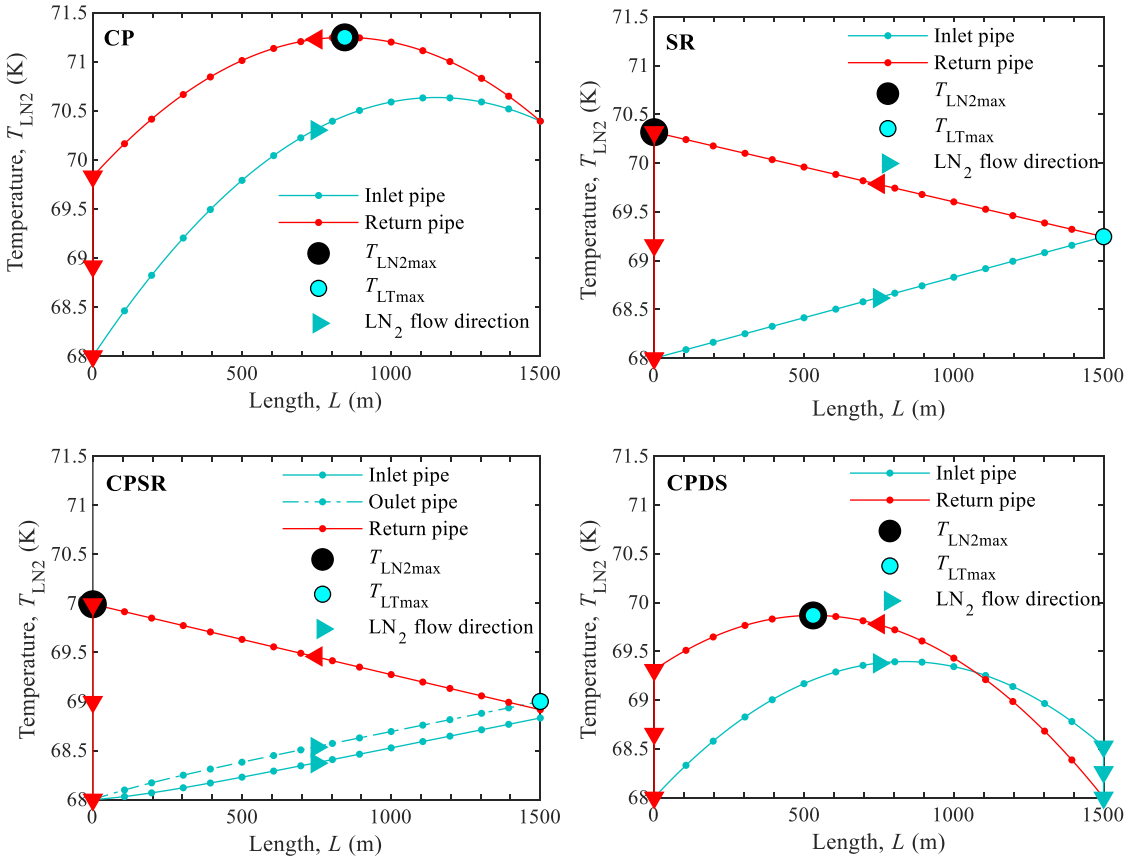

Figure 15. Temperature distribution of a cable as a function of length for different cooling configurations CP SP, CPSR and CPDS, the mass flow rate is 0.6 kg/s and the cryostat surface loss is 3 W/m^2.

Table 4. Parameters of the studied cable.

Description	Value		Property
Former	32 (mm)		Diameter
HTS tapes	0.2 (mm)		Thickness
Electrical Insulation PPLP	6 (mm)		Thickness
Internal cryostat	CP	65 (mm)	Diameter
	SP	50 (mm)	
	CPSR	65 (mm)	
	CPDS	65 (mm)	
Outer cryostat	CP	100 (mm)	Diameter
	SP	80 (mm)	
	CPSR	100 (mm)	
	CPDS	100 (mm)	
External cryostat (return pipe)	CP	***	Diameter
	SP	65 (mm)	
	CPSR	65 (mm)	
	CPDS	***	
Cable length	1500 (m)		Length

As mentioned before, the main constraints of the design are the maximum temperature in contact with the tape T_{LTmax} for the choice of the critical current and the maximum temperature of the liquid nitrogen T_{LN2max} to ensure the cooling of the cable in steady state. Additionally, these two parameters depend on the choice of the cooling type. For the CP and CPDS types, the two temperatures T_{LTmax} and T_{LN2max} are the same, but for the SP and CPSR types, the two temperatures are at the ends of the cable. This is due to the fact that the return of liquid nitrogen is provided by an external cryostat that does not contain a superconducting tape. In addition, the two temperatures T_{LTmax} and T_{LN2max} are not accessible for measurement for the CP and

Table 5. Physical parameters used in the simulations.

Material	Parameter	Value
LN_2	C_p (J.kg^{-1}.K^{-1})	2010
	ρ (kg.m^{-3})	811
	μ (10^{-6}Pa.s)	160
HTS	k (W.m^{-1}.K^{-1})	150
PPLP	k (W.m^{-1}.K^{-1})	0.15
Copper	k (W.m^{-1}.K^{-1})	528
Stainless steel	k (W.m^{-1}.K^{-1})	1

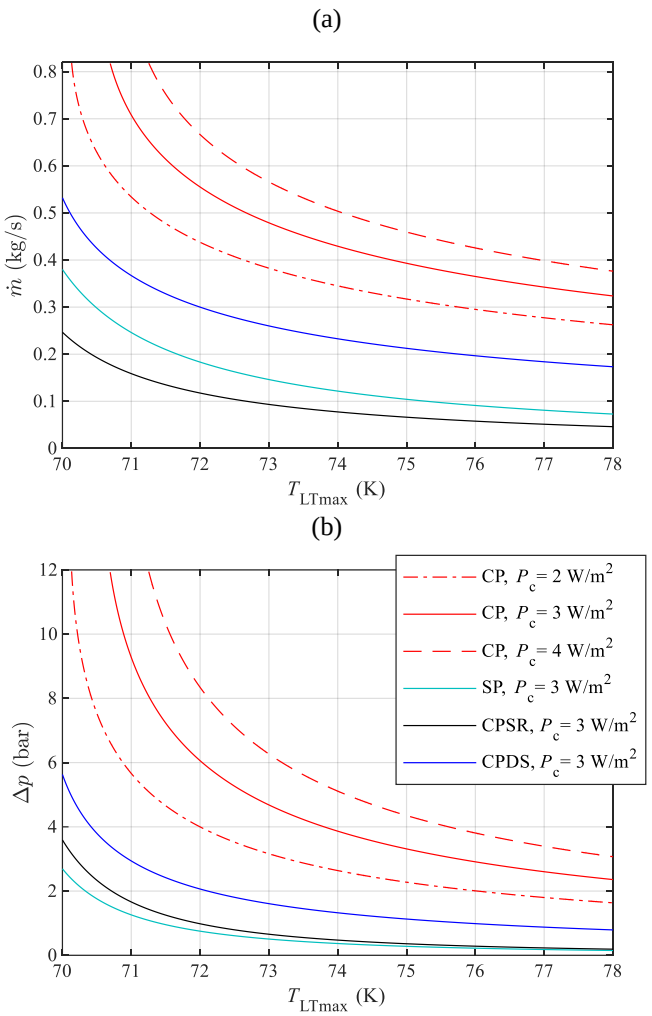

Figure 16. (a) The mass flow rate $\dot{m}$, (b) Pressure drop Δp as a function of the maximum temperature in contact with the tape for a diameter according to DIN10380 equal to 32 mm and for several cooling topologies. The cable length L is 1500 m.

CPDS configurations. From the cooling point of view, the CPxx pipes require a less powerful cooling system than the SP. This is simply explained by the difference in temperature of the liquid nitrogen ΔT_{LN2} at the cooling station (z = 0). Indeed, the ΔT_{LN2} is equal to 1.83, 1.99 and 0 for the CP, CPSR and CPDS pipes respectively whereas the ΔT_{LN2} is equal to 2.31 K in SP. From the thermal point of view, we can see that the CP configuration has the highest T_{LN2max} than the other configurations for the same mass flow rate, this allows us to interpret that the CP requires a more powerful nitrogen circulation pump.

4.4 Choice of cooling configuration

In this section, we discuss the advantages and limitations of each cooling configuration for superconducting cables. The main parameter for choosing the best type of cooling is the liquid nitrogen flow rate, however, this cannot be increased indefinitely, the mass flow rate $\dot{m}$, in addition to being limited by the capacity of the station is constrained by the pressure drop in the pipe. In this study, the length of the cable is 1500 m, the external section of the pipe of the configurations in CPxx to was chosen equal to the internal section of the pipe, the former diameter is equal to 32 mm. Figure 16(a) and (b) shows the evolution of the mass flow rate and pressure drop as a function of T_{LTmax} for different cooling configurations with the same surface losses of the cryostat P_c = 3 W/m^2. From a hydraulic point of view, the SP configuration has better performances than the CPxx configuration, indeed the regular pressure drops are much lower, as example, for a T_{LTmax} of 72 K, the SP generates about 0.75 bar whereas the CP, CPSR and CPDS generate 6.04 bar, 0.94 bar and 2.06 bar, respectively. This result is explained by the fact that the external pipe of the CPxx architecture is annular, which means that the surface in contact with the fluid generating the friction is larger for the same section. On the other hand, we notice that the CP requires a higher nitrogen flow rate than the CPSR, SP and CPDS configurations. As an example, to maintain a T_{LTmax} equal to 71 K, the mass flow is equal to 0.70 kg/s for CP and equal to 0.16 kg/s, 0.24 kg/s and 0.37 kg/s for the CPSR, SP, and CPDS.

The value of the cryostat surface loss has a major impact on the cryogenic heat load. Indeed, the reduction of P_c allows to decrease the power of the nitrogen circulation pumps, and consequently to reduce the pressure losses in the cable. As a result, a 1 W/m^2 reduction in cryostat heat loss can reduce system heat loads by several kilowatts for long cables. Indeed, to maintain a maximum temperature in contact with the tapes of 72 K, the thermal load related to loading losses is equal to 0.75 kW, 0.41 kW and 0.21 kW and the thermal load related to cryostat losses is equal to 3.77 kW, 2.82 kW and 1.88 kW for cryostat losses P_c equal to 4 W/m^2, 3 W/m^2, 2 W/m^2 respectively.

We can therefore conclude that the main obstacle limiting the concentric architecture is the pressure drop, we note that the pressure drops are strongly influenced by the pipe diameter. Moreover, the CP configuration generates much more pressure drop than the other configurations, so this configuration is more reliable for short lengths. On the other hand, the CPDS provides good cooling of the cable for longer lengths, but this type of cooling requires two cooling systems at each end of the cable.

The SP configuration has negligible pressure drop compared to CPxx configurations. Besides, in a bipolar cable, cooling is only provided by the inner pipe, which can cause troubles in case of fault. Indeed, the electrical insulation between the two poles is an obstacle for the cable cooling, as only the inner pole will be properly cooled leading to an increase in the recovery time.

The CPSR is still the best choice for long cables, although it requires us to add a second external duct for the nitrogen return,

which would generate additional heat losses and increase the cost of the installation.

4.5 Optimization and discussion

Based on the models presented above, the optimization method was applied to size the superconducting DC cables. In this study, the cable has a length of 1500 m, its carrying current must be superior to 10 kA, the voltage of the railway network is equal to 1500 V. Figure 17 shows a bi-objective optimization result between the total length of the tape used and the cable losses for the CP configuration. Each group of dots represents the possible solutions for a single standardized former diameter and each number next to a solution represents the number of layers per pole of the cable. First, we can clearly see that increasing the number of layers per pole leads to a growth in the total length of the tapes to be used, while increasing the radius of the inner pipe leads to higher losses in the cryostat. This allows us to conclude that there is a trade-off between these two parameters to determine the optimum cable solution.

For the same cable parameters shown above, figure 18 shows the Pareto fronts of the four cooling configurations. It can be seen that the CPSR and SP lines with a separate return generate more losses than the concentric CP and CPDS configuration. This is because CPSR and SP have an external cryostat that ensures the return of nitrogen, moreover, CPSR produces more losses than SP, and this is because CPSR has a larger external cryostat diameter than SP. On the other hand, the CPDS generates less loss than the CP, this being explained by the fact that the CPDS requires a lower flow of nitrogen than the CP, it thus generates fewer hydraulic losses.

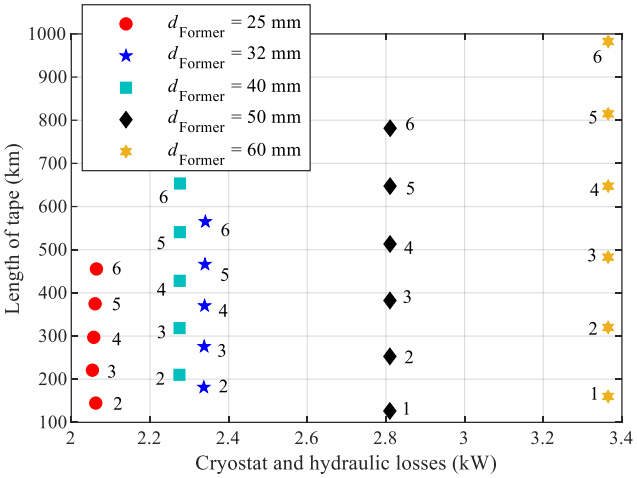

Figure 17. Bi-objective optimization between the total length of the tape and the cable losses, the transport current is greater than 10 kA, the type of cooling is CP and the cable length L is equal to 1500 m. Each number next to a solution represents the number of layers per pole of the cable.

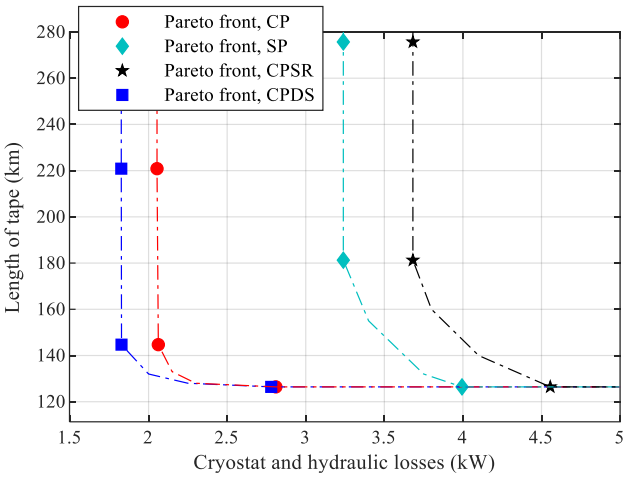

Figure 18. Optimal solution, Pareto front of total used tape length versus cable losses for four cooling configurations CP, SP, CPSR and CPDS. The transport current is greater than 10 kA, the cable length is 1500 m.

5. Conclusion

In this paper, a set of tools for the design of DC superconducting cables has been presented. This method contains a 3D electromagnetic analytical model based on the scalar magnetic potential to account for the 3D effects related to the torsion of the tape and to minimize the computational cost. In order to ensure the cooling of the superconducting cables and to consider the dependence of the critical current on the temperature I_c ($B_{//}, B_{\perp}, T$), thermal and hydraulic models have been presented and evaluated for the four types of cooling that can be used in a real case. This allows us to determine the dimensioning parameters of the nitrogen circulation pump as well as the cooling system power. Indeed, the length of the cable has a significant impact on the cooling capacity. The proposed optimization process also allows us to find a comparison between the total length of tapes and the cable losses. Moreover, the algorithm allows calculating the diameter of the cryogenic tubes according to the DIN EN 10380 standard. Thus, from the industrial data of the characteristics of the high-temperature superconducting tapes and the cryogenic data, the algorithm allows having standardized solutions that exist on the European and international market.

6. Nomenclature

Parameter	Unit	Description
r	m	Coordinate in the radial direction (in index, means component along r)
θ	rad	Coordinate in the azimuthal direction (in index, means component along θ)

z	m	Coordinate in the axial direction (in index, means component along z)
d	mm	Tape width
d_e	mm	Gap between two tapes
a	mm	Radius where the tape is located
z_L	mm	Twist pitch
α_z	mm	Apparent width of the tape
β_z	mm	Axial pitch of the tape
β_θ	rad/m	Angular pitch
m	rad/m	Twist parameter
δ	rad	Twist angle
th_{Tape}	mm	Thickness of HTS tape
th_{PPLP}	mm	Thickness of electrical insulation PPLP
th_p	mm	Thickness of the former
e_i	mm	Thickness of all layers (positive and negative poles) and electrical insulation
k, n'	---	Harmonic rank
N_b	---	Harmonic number
ϑ	---	Index to define the study of the positive or negative pole
$\mathbb{R}^3$	m^3	Entire space
R_F	mm	Radius of the former normalized (DIN EN 10380)
R_g	mm	Radius of each conductor
R_e	mm	Radius of the outer pipe
R_{DIN}/d_{DIN}	mm	Standard radius/ diameter (DIN EN 10380)
R_{OutDIN}	mm	Radius of the external pipe normalized (DIN EN 10380)
R_c	mm	Outer radius of the cable (DIN EN 10380)
R_{lim}	mm	Radius limit of the integral
n	---	Number of layers per pole
N	---	Number of tapes per layer and per pole
N_t	---	Number of tapes per layer
I_c	A	Critical current
I_n	A	Cable current rating
I	A	Single tape current
Φ	A/m^2	Magnetic scalar potential
B	T	Magnetic induction
$B_{/\!/}$	T	Magnetic induction parallel to the a, b plane of the HTS tape
$B_\perp$	T	Magnetic induction perpendicular to the a, b plane of the HTS tape.
H	A/m	Magnetic field
W_m	J	Magnetic energy
J_s	A/m	Surface current density
$J_{s,zMax}$	A/m	Maximum value of the surface current density in the axial direction
$J_{s,\theta Max}$	A/m	Maximum value of the surface current density in the azimuthal direction
L_i	H	Self-inductance
L_{ij}	H	Mutual inductance
L_{Layer}	H/m	Self-inductance of a layer per pole per unit length
μ_0	H/m	Relative permeability
k_a	---	Anisotropy factor
B_0	T	Constants that characterize the variation of I_c vs B
σ	---	Constants that characterize the variation of I_c vs B
I_{c0}	A	Critical current under zero field
$I_{c0,68\ K}$	A	Critical current under zero field at 68 K
L	m	Cable length
Ψ_H	W	Hydraulic losses
Ψ_P	W	Cryostat losses
P_c	W/m^2	Surface loss of the cryostat
ζ_p	W/m^2	Half of the surface loss of the cryostat
p	bar	Pressure
$\dot{m}$	Kg/s	Mass flow rate
D_H	mm	Hydraulic diameter
C_p	$J/kg/m^3$	Specific heat of the fluid (liquid nitrogen)
G_0	W/m/K	Equivalent thermal conductance per unit length
H_a	m	Altitude on the liquid nitrogen path
h	$W/m^2/K$	Coefficient of thermal convection
k	W/m/K	Thermal conductivity
ρ	Kg/m^3	Density of the fluid (liquid nitrogen)
μ	Pa/s	Viscosity of the fluid (liquid nitrogen)
χ_H	J/Kg	Hydraulic loss factor
T_i	K	Temperature of the inner pipe (former)
T_o	K	Temperature of the outer pipe
T_u	K	Temperature of the nitrogen return pipe
T_{LN2}	K	Temperature of liquid nitrogen
T_{LTmax}	K	Maximum temperature in contact with the tape

T_{LN2max}	K	Maximum temperature of liquid nitrogen
T_c	K	Critical temperature of HTS tape
$T_i(0)$	K	Initial temperature of the liquid nitrogen
g	---	Index of the layer per pole
i	---	Index of the inner pipe
o	---	Index of the outer pipe
s	---	Index of the external pipe
u	---	Index of the return pipe
q	---	Index of each cable element
ΔT_{LN2}	K	Temperature difference between liquid nitrogen inlet and outlet at ($z = 0$)
$\Delta\varphi$	rad	Angular pitch between two tapes
Δp	bar	Pressure drop
I_k	---	Modified Bessel functions of first kind
K_k	---	Modified Bessel functions of the second kind
I'_k	---	Derivative of modified Bessel functions of the first kind
K'_k	---	Derivative of modified Bessel functions of the second kind

Appendix A. 3D variable separation method for the determination of the general solution of the magnetic scalar potential

For the two regions *I* and *II*, the Laplace equation in the 3D cylindrical coordinate system is as follows:

$$\frac{d^2\Phi^i}{dr^2}+\frac{1}{r}\frac{d\Phi^i}{dr}+\frac{1}{r^2}\frac{d^2\Phi^i}{d\theta^2}+\frac{d^2\Phi^i}{dz^2}=0 \tag{A.1}$$

The analytical model is based on the solution of the Laplace equation (1) by the separation of variables method. We separate the variables according to (r, θ, z), we define:

$$\Delta\Phi^i = f_i(r)g_i(\theta)h_i(z) \tag{A.2}$$

From expressions 1 and 3, we separate the variables and introduce two separation constants ε and λ.

$$\frac{1}{r^2}\frac{g_i(\theta)''}{g_i(\theta)}=\varepsilon \tag{A.3}$$

$$\frac{h_i(z)''}{h_i(z)}=\gamma \tag{A.4}$$

$$\frac{f_i(r)''}{f_i(r)}+\frac{1}{r}\frac{f_i(r)'}{f_i(r)}=-\frac{\varepsilon}{r^2}-\gamma \tag{A.5}$$

Then, we pose the following three second-order differential equations, we solve the eigenvalue problem by treating all possible cases as shown in table 6.

The general solution of the scalar potential in the two regions are in the form:

$$\begin{aligned}\Phi^I = {} & A_{00}^I + \sum_{k=1}^{\infty} A_{0k}^I r^k \left(A_{0k}^I \cos(k\theta) + B_{0k}^I \sin(k\theta)\right) + \\ & \sum_{n'=1}^{\infty} E_{n0}^I I_0\left(\frac{2\pi\, n'}{z_L}r\right)\left(A_{n0}^I \cos\left(\frac{2\pi\, n'}{z_L}\, z\right) + B_{n0}^I \sin\left(\frac{2\pi\, n'}{z_L}z\right)\right) + \\ & \sum_{n'=1}^{\infty}\sum_{k=1}^{\infty} I_k\left(\frac{2\pi\, n'}{z_L}r\right)\left(V_1^I \cos(k\theta)\cos\left(\frac{2\pi\, n'}{z_L}\, z\right) + V_2^I \cos(k\theta)\sin\left(\frac{2\pi\, n'}{z_L}\, z\right) + V_3^I \sin(k\theta)\cos\left(\frac{2\pi\, n'}{z_L}\, z\right) + V_4^I \sin(k\theta)\sin\left(\frac{2\pi\, n'}{z_L}\, z\right)\right)\end{aligned} \tag{A.6}$$

$$\begin{aligned}\Phi^{II} = {} & A_{00}^{II} \ln(r) + \sum_{k=1}^{\infty} A_{0k}^{II} r^{-k} \left(A_{0k}^{II} \cos(k\theta) + B_{0k}^{II} \sin(k\theta)\right) + \\ & \sum_{n'=1}^{\infty} E_{n0}^{II} K_0\left(\frac{2\pi\, n'}{z_L}r\right)\left(A_{n0}^{II} \cos\left(\frac{2\pi\, n'}{z_L}\, z\right) + B_{n0}^{II} \sin\left(\frac{2\pi\, n'}{z_L}z\right)\right) + \\ & \sum_{n'=1}^{\infty}\sum_{k=1}^{\infty} K_k\left(\frac{2\pi\, n'}{z_L}r\right)\left(V_1^{II} \cos(k\theta)\cos\left(\frac{2\pi\, n'}{z_L}\, z\right) + V_2^{II} \cos(k\theta)\sin\left(\frac{2\pi\, n'}{z_L}\, z\right) + V_3^{II} \sin(k\theta)\cos\left(\frac{2\pi\, n'}{z_L}\, z\right) + V_4^{II} \sin(k\theta)\sin\left(\frac{2\pi\, n'}{z_L}\, z\right)\right)\end{aligned} \tag{A.7}$$

Appendix B. Determination of the unknown coefficients for the harmonic terms

In this part, we determine the expressions of the magnetic field from the relation (2), then from the passing conditions (10), (11) and (12). We determine the expressions of the coefficients of the three magnetic field components in each region. From the conditions of passage to ($r = a$). We see first

Table 6. The different possible cases of the general solution.

Separation constants	Value			
	Case1	Case2	Case3	Case4
ε	0	1	0	1
γ	0	0	1	1

that the term ($k \neq 0$ and $n' = 0$) and ($n' \neq 0$ and $k = 0$) are not a solution.

$$A_{0k}^{I} = A_{0k}^{II} = 0 \quad \text{(B.1)}$$

$$E_{n0}^{I} = E_{n0}^{II} = 0 \quad \text{(B.2)}$$

moreover, it is necessary that n' and k are equal to consider a possible solution. Hence, we obtain:

$$V_2^I = V_3^I = V_2^{II} = V_3^{II} = 0 \quad \text{(B.3)}$$

$$V_1^I = \frac{2\mu_0 NI}{n'\pi}\frac{K_k(m\,a)}{d}\frac{k}{m}cos(\delta)sin\left(\frac{\alpha}{\beta}\pi n'\right) \quad \text{(B.4)}$$

$$V_1^I = V_4^I \quad \text{(B.5)}$$

$$V_2^{II} = \frac{2\mu_0 NI}{n'\pi}\frac{I_k(m\,a)}{d}\frac{k}{m}cos(\delta)sin\left(\frac{\alpha}{\beta}\pi n'\right) \quad \text{(B.6)}$$

$$V_2^{II} = V_3^{II} \quad \text{(B.7)}$$

The properties of the modified Bessel function used here to solve the system of equations are:

$$I_v(\omega)K_{v+1}(\omega) + I_{v+1}(\omega)K_v(\omega) = \frac{1}{\omega} \quad \text{(B.8)}$$

The relations used of the higher-order Bessel functions and their derivative for all real values of v are formulated as follows:

$$I_v'(\omega) = \frac{v}{\omega}I_v(\omega) + I_{v+1}(\omega) \quad \text{(B.9)}$$

$$K_v'(\omega) = \frac{v}{\omega}K_v(\omega) - K_{v+1}(\omega) \quad \text{(B.10)}$$

References

[1] Pietzcker R C, Longden T, Chen W, Fu S, Kriegler E, Kyle P and Luderer G 2014 Long-term transport energy demand and climate policy: Alternative visions on transport decarbonization in energy-economy models *Energy* **64** 95–108

[2] Tomita M, Fukumoto Y, Ishihara A, Suzuki K, Akasaka T, Caron H, Kobayashi Y and Onji T 2020 Train Running Test Transmitted by Superconducting Feeder Cable and Study as an Example of Line in Japan and France *IEEE Transactions on Applied Superconductivity* **30** 1–7

[3] Tomita M, Suzuki K, Fukumoto Y, Ishihara A and Muralidhar M 2011 Next generation of prototype direct current superconducting cable for railway system *Journal of Applied Physics* **109** 063909

[4] Tomita M, Muralidhar M, Suzuki K, Fukumoto Y and Ishihara A 2012 Development of 10 kA high temperature superconducting power cable for railway systems *Journal of Applied Physics* **111** 063910

[5] Sytnikov V E, Vysotsky V S, Rychagov A V, Polyakova N V, Radchenko I P, Shutov K A, Lobanov E A and Fetisov S S 2007 The 5 m HTS Power Cable Development and Test *IEEE Transactions on Applied Superconductivity* **17** 1684–7

[6] Amemiya N, Li Q, Ito K, Takeuchi K, Nakamura T and Okuma T 2011 Ac loss reduction of multilayer superconducting power transmission cables by using narrow coated conductors *Supercond. Sci. Technol.* **24** 065013

[7] Wang Y, Zhang M, Grilli F, Zhu Z and Yuan W 2019 Study of the magnetization loss of CORC ® cables using a 3D T-A formulation *Supercond. Sci. Technol.* **32** 025003

[8] Klöppel S, Marian A, Haberstroh C and Bruzek C-E 2021 Thermo-hydraulic and economic aspects of long-length high-power MgB2 superconducting cables *Cryogenics* **113** 103211

[9] Stemmle M, Merschel F, Noe M and Hobl A 2014 AmpaCity — Advanced superconducting medium voltage system for urban area power supply *2014 IEEE PES T D Conference and Exposition* 2014 IEEE PES T D Conference and Exposition pp 1–5

[10] de Sousa W T B, Polasek A, Dias R, Matt C F T and de Andrade R 2014 Thermal–electrical analogy for simulations of superconducting fault current limiters *Cryogenics* **62** 97–109

[11] Hajiri G, Berger K, Dorget R, Lévêque J and Caron H 2021 Thermal and Electromagnetic Design of DC HTS Cables for the Future French Railway Network *IEEE Transactions on Applied Superconductivity* **31** 1–8

[12] Vyatkin V S, Tanabe K, Wada J, Kiuchi M, Otabe E S and Matsushita T 2013 Calculation of critical current in DC HTS cable using longitudinal magnetic field effect *Physica C: Superconductivity* **494** 135–9

[13] Tominaka T 2006 Magnetic field calculation of an infinitely long solenoid *Eur. J. Phys.* **27** 1399–408

[14] Tominaka T 2005 Inductance calculation for helical conductors *Supercond. Sci. Technol.* **18** 214–22

[15] Tominaka T 2009 Inductance calculation of twisted conductors by the broken line approximation *Cryogenics* **49** 94–102

[16] Tominaka T 2008 Self- and mutual inductances of long coaxial helical conductors *Supercond. Sci. Technol.* **21** 015011

[17] Tomita M, Suzuki K, Fukumoto Y, Ishihara A, Akasaka T and Kobayashi Y 2017 Energy-saving railway systems based on superconducting power transmission *Energy* **122** 579–87

[18] de Sousa W T B, Shabagin E, Kottonau D and Noe M 2021 An open-source 2D finite difference based transient electro-thermal simulation model for three-phase concentric superconducting power cables *Supercond. Sci. Technol.* **34** 015014

[19] Masood A, Zuberi M U and Husain E 2008 Breakdown strength of solid dielectrics in liquid nitrogen *IEEE Transactions on Dielectrics and Electrical Insulation* **15** 1051–5

[20] Sotelo G G, Carrera M, Lopez-Lopez J and Granados X 2016 H-Formulation FEM Modeling of the Current Distribution in 2G HTS Tapes and Its Experimental Validation Using Hall Probe Mapping *IEEE Transactions on Applied Superconductivity* **26** 1–10

[21] Lee S, Petrykin V, Molodyk A, Samoilenkov S, Kaul A, Vavilov A, Vysotsky V and Fetisov S 2014 Development and production of second generation high T_c superconducting tapes at SuperOx and first tests of model cables *Supercond. Sci. Technol.* **27** 044022

[22] Sundaram A, Zhang Y, Knoll A R, Abraimov D, Brownsey P, Kasahara M, Carota G M, Nakasaki R, Cameron J B, Schwab G, Hope L V, Schmidt R M, Kuraseko H, Fukushima T and Hazelton D W 2016 2G HTS wires made on 30 μ m thick Hastelloy substrate *Supercond. Sci. Technol.* **29** 104007

[23] Zhang H, Zhang M and Yuan W 2017 An efficient 3D finite element method model based on the *T–A* formulation for superconducting coated conductors *Supercond. Sci. Technol.* **30** 024005

[24] Lubin T and Rezzoug A 2017 Improved 3-D Analytical Model for Axial-Flux Eddy-Current Couplings With Curvature Effects *IEEE Transactions on Magnetics* **53** 1–9

[25] Shabagin E, Heidt C, Strauß S and Grohmann S 2017 Modelling of 3D temperature profiles and pressure drop in concentric three-phase HTS power cables *Cryogenics* **81** 24–32

[26] Herzog F, Kutz T, Stemmle M and Kugel T 2016 Cooling unit for the AmpaCity project – One year successful operation *Cryogenics* **80** 204–9

[27] Smith N F 1972 Bernoulli and Newton in Fluid Mechanics *The Physics Teacher* **10** 451–5

[28] Trinh K T 2010 On the Blasius correlation for friction factors *arXiv:1007.2466 [physics]*

[29] Gouge M J, Demko J A, Roden M L, Maguire J F and Weber C S 2008 Vacuum-insulated, flexible cryostats for long hts cables: requirements, status and prospects *AIP Conference Proceedings* **985** 1343–50

[30] Samoilenkov S, Molodyk A, Lee S, Petrykin V, Kalitka V, Martynova I, Makarevich A, Markelov A, Moyzykh M and Blednov A 2016 Customised 2G HTS wire for applications *Supercond. Sci. Technol.* **29** 024001

[31] Berger K, Leveque J, Netter D, Douine B and Rezzoug A 2007 Influence of Temperature and/or Field Dependences of the $E-J$ Power Law on Trapped Magnetic Field in Bulk YBaCuO *IEEE Transactions on Applied Superconductivity* **17** 3028–31

[32] Wimbush, Stuart and Strickland, Nick 2021 A high-temperature superconducting (HTS) wire critical current database

[33] Wimbush S C and Strickland N M 2017 A Public Database of High-Temperature Superconductor Critical Current Data *IEEE Trans. Appl. Supercond.* **27** 1–5

[34] Solovyov M, Pardo E, Šouc J, Gömöry F, Skarba M, Konopka P, Pekarčíková M and Janovec J 2013 Non-uniformity of coated conductor tapes *Supercond. Sci. Technol.* **26** 115013

[35] Sytnikov V E, Dolgosheev P I, Svalov G G, Polyakova N V and Belij D I 1998 Influence of the multilayer HTS-cable conductor design on the current distribution *Physica C: Superconductivity* **310** 387–91

[36] Zhu J, Zhang Z, Zhang H, Zhang M, Qiu M and Yuan W 2014 Inductance and Current Distribution Analysis of a Prototype HTS Cable *J. Phys.: Conf. Ser.* **507** 022047

[37] Sytnikov V E, Poliakova N V and Vysotsky V S 2004 Current distribution and voltage–current relation in multi-layered LTS and HTS power cable core: a review *Physica C: Superconductivity* **401** 47–56

[38] Vyatkin V S, Kiuchi M, Otabe E S and Matsushita T 2015 Design of Practical Superconducting DC Power Cable With REBCO Coated Conductors *IEEE Transactions on Applied Superconductivity* **25** 1–7